The Dissociation Rate of Acetylacetonate Ligands Governs the Size of Ferrimagnetic Zinc Ferrite Nanocubes

Aidin Lak,*,[†]◉ Tamara Kahmann,[‡] Simon Jakob Schaper,[¶] Jaroslava Obel,[§] Frank Ludwig,[‡] Peter Müller-Buschbaum,[¶]◉ and Jan Lipfert*,[†]◉

[†]Department of Physics and Center for NanoScience, LMU Munich, Amalienstr. 54, 80799 Munich, Germany

[‡]Institute for Electrical Measurement Science and Fundamental Electrical Engineering, Technische Universität Braunschweig, Hans-Sommer-Str. 66, 38106 Braunschweig, Germany

[¶]Lehrstuhl für Funktionelle Materialien, Physik-Department, Technische Universität München, James-Franck-Str. 1, 85748 Garching, Germany

[§]Department of Chemistry and Pharmacy, Analytical Division, LMU Munich, Butenandtstr. 5-13, 81377 Munich, Germany

Ⓢ *Supporting Information*

ABSTRACT: Magnetic nanoparticles are critical to a broad range of applications from medical diagnostics and therapeutics to biotechnological processes and single-molecule manipulation. To advance these applications, facile and robust routes to synthesize highly magnetic nanoparticles over a wide size range are needed. Here, we demonstrate that changing the degassing temperature of thermal decomposition of metal acetylacetonate precursors from 90 to 25 °C tunes the size of ferrimagnetic $Zn_xFe_{3-x}O_4$ nanocubes from 25 to 100 nm, respectively. We show that degassing at 90 °C nearly entirely removes acetylacetone ligands from the reaction, which results in an early formation of monomers and a reaction-controlled growth following LaMer's model toward small nanocubes. In contrast, degassing at 25 °C only partially dissociates acetylacetone ligands from the metal center and triggers a delayed formation of monomers, which leads to intermediate assembled structures made of tiny irregular crystallites and an eventual formation of large nanocubes via a diffusion-controlled growth mechanism. Using complementary techniques, we determine the substitution fraction x of Zn^{2+} to be in the range of 0.35−0.37. Our method reduces the complexity of the thermal decomposition method by narrowing the synthesis parameter space to a single physical parameter and enables fabrication of highly magnetic and uniform zinc ferrite nanocubes over a broad size range. The resulting particles are promising for a range of applications from magnetic fluid hyperthermia to actuation of macromolecules.

KEYWORDS: *magnetic nanoparticles, zinc ferrite nanocubes, size-controlled synthesis, degassing temperature, acetylacetonate ligands, growth mechanism, ¹H NMR spectroscopy*
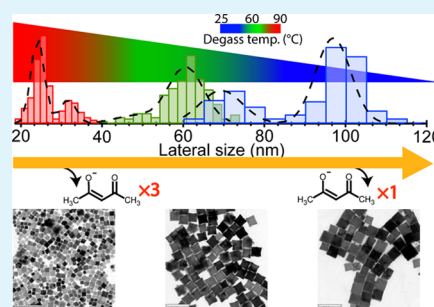
■ INTRODUCTION

Magnetic nanoparticles show great promise for a range of biomedical applications such as magnetic fluid hyperthermia (MFH), targeted drug delivery, magnetic resonance imaging (MRI), and magnetic particle imaging.[1−6] The colloidal synthesis of nanoparticles via thermal decomposition of organometallic precursors has significantly advanced nano-particle-based technologies, as it offers an excellent control over particle size and shape distribution and crystallinity.[7−15] Particles with different sizes and magnetic properties are needed depending on the application in mind. Although 25 nm nanoparticles are suitable for magnetic hyperthermia,[16] few hundred nanometers large particles are required for cell separation and magnetic tweezers assays to manipulate cells and macromolecules.[17−20]

Size-controlled synthesis of magnetic nanoparticles up to hundreds of nanometers has been reported previously.[13,14] Recently, there has been a shift toward synthesizing anisotropically shaped magnetic particles such as cubic,[21−27]

octapod-,[28,29] and flower-shaped[30] particles instead of spheres. Anisotropic particles have a larger magnetic anisotropy due to an additional contribution from shape anisotropy, a more defined magnetization axis, and a larger surface-to-volume ratio than spherical particles with equal volume.[31] In most studies, a combination of chemical synthesis parameters such as the capping ligands and external synthesis parameters like the heating rate was exploited to achieve a wide size range. For instance, in their pioneering work, Hyeon and co-workers[13] have synthesized 160 nm iron oxide nanocubes through thermal decomposition of iron(III) acetylacetonate applying a high heating rate. They have also demonstrated that the particle size reduces to 22 nm if 4-biphenylcarboxylic acid is used in addition to oleic acid. Guardia et al.[14] have shown that the decomposition of the same precursor in the presence of

decanoic acid results in large particles only if the heating rate is reduced, in contrast to the results by Hyeon and co-workers.[13] A size increase by applying either higher[32] or lower[33] heating rates has been shown for other magnetic binary oxides. In general, the synthesis parameter space of the thermal decomposition method is large and complicated, often resulting in poor reproducibility of the synthesis. In addition, our understanding of the underlying mechanisms through which large nanocubes are formed remains limited.[34]

The emergence of iron oxide nanocubes has enabled considerable advancements in, for example, MRI and MFH, yet there is still a high demand for particles with larger magnetization.[15,16,23,35,36] Approaches to improving the magnetic properties of iron oxide nanoparticles include modifying the reaction's protective gas or the nature of the solvent.[37−40] However, a more efficient strategy to enhance the saturation magnetization is the replacement of Fe^{3+} with Zn^{2+} in tetrahedral sites of magnetite.[41−44] Although zinc is nonmagnetic, its doping increases the overall magnetization of iron oxide nanoparticles by reducing the antiferromagnetic coupling of Fe^{3+} spins between octahedral and tetrahedral sites through superexchange interactions. However, the optimal level of doping x of Zn^{2+} into the tetrahedral sites of the $Zn_xFe_{3−x}O_4$ structure is still controversial.[42,45,46] In summary, the synthesis of nanocubes with optimized magnetic properties and good size control is very promising to advance nanoparticle-based technologies, but it remains poorly understood.

Here, we demonstrate that the kinetics of colloidal synthesis of $Zn_xFe_{3−x}O_4$ via thermal decomposition of metal acetylacetonate is governed by dissociation of acetylacetonate ligands and their availability in the reaction. We show that the particle size increases with decreasing degassing temperature due to an increase in the acetylacetone content of the reaction mixture. The final particles preserve their size uniformity and cubicity regardless of the degassing temperature. We employ complimentary characterization techniques to provide evidence that smaller nanocubes form through a reaction-controlled growth model, whereas large nanocubes grow through assembly of small crystallites into assembled structures and eventual formation of cubic particles, following a diffusion-controlled growth pathway. Our work provides both mechanistic insights and a straightforward and robust way of synthesizing uniform and highly magnetic zinc ferrite nanocubes suitable for a broad range of biomedical applications.

■ EXPERIMENTAL SECTION

Chemicals. Iron(III) acetylacetonate (99.8%, metal trace), dibenzyl ether (DBE, 98%), oleic acid (OA, 90%), DMSO-d_6 (99.5 at. % D), $CDCl_3$ (99.8 at. % D), and solvents with the highest purity grade were purchased from Sigma-Aldrich. Oleic acid (99%) was purchased from TCI, America. Zinc(II) acetylacetonate (95%) was purchased from Merck. The chemicals were utilized without further purification.

Synthesis of Nanocubes. In a typical synthesis and to obtain 60 nm zinc ferrite nanocubes, 1 mmol (0.353 g) of iron(III) acetylacetonate, 1 mmol (0.263 g) of zinc(II) acetylacetonate, 10 mL of DBE, and 4 mmol (1.26 mL) of oleic acid were added into a 50 mL three-neck glass flask, equipped with a thermometer and connected to a Schlenk line through a condenser. The mixture was degassed at 60−70 °C and 30 μbar reducing pressure for 1 h using Schlenk techniques. Afterward, the flask was filled with N_2, and the mixture was heated up to 130 °C at a heating ramp rate of 4 °C/min and kept for 5 min to thoroughly homogenize the mixture.

Subsequently, the mixture was heated up to 290 °C at a heating ramp rate of 20 °C/min and aged at this temperature for 30 min. After cooling the flask to 80 °C, the black viscous product was diluted and dispersed by adding 20 mL of chloroform. The formed particles were precipitated by adding 50 mL of acetone and centrifuging at 7000 rpm for 10 min. After each centrifugation step, the collected particles were dispersed in 20 mL of chloroform through vigorous sonication for 10 min. The washing procedure was repeated five more times to remove organic species and obtain clean particles. Finally, the particles were dispersed in 20 mL of chloroform and stored at room temperature (RT) for further use and characterization. To reduce the particle aggregation and preserve the colloidal stability of the particles during the storage period, 500 μL of oleic acid was added to the suspension. The synthesis experiments for ^{1}H NMR and FTIR analyses were carried out using oleic acid with 99% purity.

To obtain 25 and 100 nm nanocubes, the degassing temperature was set to 90 and 25 °C, respectively, and other synthesis parameters were kept exactly the same.

Transmission Electron Microscopy (TEM). TEM micrographs were acquired on a JEOL JEM-1011 microscope operated at 80 kV. The sample was prepared by dropping a diluted particle suspension in chloroform on a 300 mesh Formvar−carbon-coated copper grid and letting it to dry thoroughly. The particle size histogram was analyzed using ImageJ software by taking more than 200 particles into the analysis.

Magnetization Measurements. Field-dependent static magnetic measurements were carried out using a Magnetic Property Measurement System (MPMS3, Quantum Design) on embedded nanoparticles. The samples were prepared by mixing 20 μL of a nanocube chloroform solution at an iron concentration of 1−2 g/L with ∼5 mg of cotton wool in designated capsules and letting it to dry thoroughly. The zero-field-cooled (ZFC) and field-cooled (FC) temperature-dependent magnetization measurements were performed on identical samples in a magnetic cooling field of 10 mT. The magnetization data were corrected with respect to the diamagnetic and paramagnetic contributions of cotton wool and capsule. The magnetization curves were normalized to the total mass of zinc ferrite nanoparticles that was estimated from the elemental analysis of zinc and iron.

Elemental Analysis. Elemental analysis was performed using an inductively coupled plasma-atomic emission spectroscopy (ICP-AES) instrument (Varian, Vista RL). Typically, 25 μL of a nanocube suspension in chloroform was digested in 1 mL of aqua regia (3 parts HCl:1 part HNO_3) in a 10 mL volumetric flask. The sample was left overnight to fully digest the particles. Afterward, the flask was filled up to the graduation mark with Milli-Q water, and the solution was filtered through a 0.2 μm filter membrane prior to the measurement.

Powder X-ray Diffraction (XRD). The XRD samples were prepared by drop casting concentrated particle suspensions on a zero diffraction silicon wafer (<100>, 10−20 Ω cm). The measurements were conducted on a D8 Advance Bruker diffractometer, equipped with Cu Kα (2.2 kW, ceramic isolation body, focus dimension 0.04 × 12 mm) rotating anode operating at 40 mA and 40 kV. The patterns were recorded in a parallel beam geometry over an angular range of 2θ = 15−95° in a step size of 0.02°.

Attenuated Total Reflection-Fourier Transform Infrared Spectroscopy (ATR-FTIR). The chemical bonds of species formed during the colloidal heat-up synthesis were probed using the ATR-FTIR technique using a PerkinElmer (Spectrum BX) instrument. The measurements were performed on the whole reaction mixture as sampled out of the reaction without further purification. In a typical measurement, a 10 μL sample drop was placed on the diamond sample holder of the instrument, and the spectrum was recorded from 650 to 4400 cm^{-1}.

^{1}H NMR Spectroscopy. The chemical structures of the substances collected in the cold trap after degassing and the reaction mixtures at the end of synthesis were analyzed using ^{1}H NMR spectroscopy (Varian). The samples were prepared by mixing typically 200 μL of sample with deuterated solvents. The spectra were recorded in $CDCl_3$ or DMSO-d_6 at 600 MHz.

■ RESULTS AND DISCUSSION

We synthesized zinc ferrite nanoparticles via a colloidal thermal decomposition of iron(III) and zinc(II) acetylacetonate precursors in a mixture of dibenzyl ether as the solvent and oleic acid as the capping ligand. Characterization of particle size and shape by transmission electron microscopy (TEM) revealed a significant and unprecedented impact of degassing temperature on particle size (Figure 1a−c). This
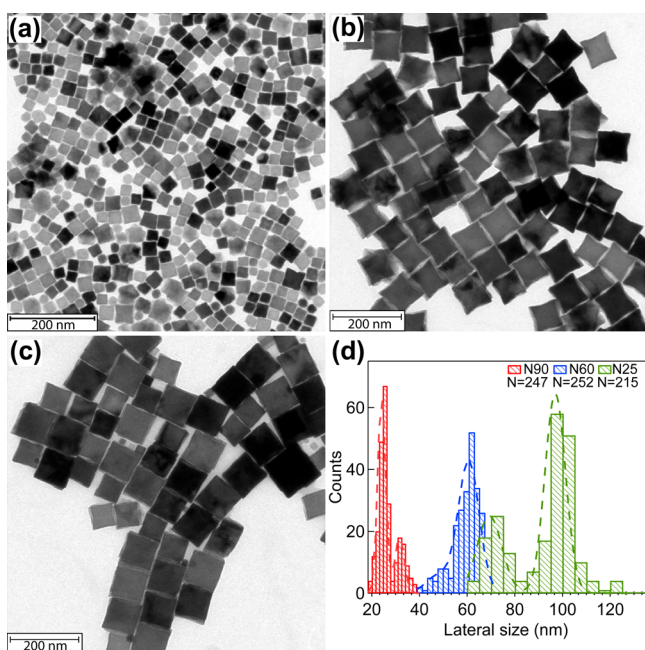

Figure 1. Transmission electron microscopy (TEM) analysis of zinc ferrite nanocubes synthesized after applying three different degassing temperatures. TEM micrographs of zinc ferrite nanocubes synthesized at 290 °C after 1 h of degassing step at (a) 90 (N90), (b) 60 (N60), and (c) 25 °C (N25). (d) Histograms of nanoparticle lateral sizes determined from analysis of the TEM images using ImageJ. Dashed lines are double Gaussian fits.

peculiar behavior motivated us to systematically tune the degassing temperature as the only variable parameter to unravel its impact on the decomposition kinetics (Figure S1a). While particles exhibited cubic shapes and overall size uniformity regardless of the degassing temperature, lower degassing temperatures gave rise to significantly larger particles. The size histograms (Figure 1d) feature a clear major fraction at each temperature as well as a minor fraction. Accordingly, we fit the distributions with a double Gaussian function. The mean particle lateral size L_{ma} of the major particle fraction increases from 24.1(0.2) to 60.6(1.3) and

96.9(0.5) nm (standard error of the mean) as the degassing temperature reduces from 90 to 60 and 25 °C. The minor fractions comprise a 30, 12, and 30% of the particles with mean sizes of 31.7(0.9), 47.2(9.5), and 69.3(1.3) nm for small, medium, and large nanocubes, respectively. The standard deviation σ of the Gaussian function fitted to the major size fractions is below 10%, indicating their size monodispersity (Table 1).

Having observed the very significant impact of the degassing temperature on the particle size, we next probed the chemistry of the decomposition reaction to understand the underlying mechanisms. First, the substances collected in cold trap during the degassing process were analyzed using ^{1}H NMR spectroscopy.

The analysis of ^{1}H NMR spectra revealed peaks at 1.89 (G), 5.36 (J), 2.09 (E), and 3.45 (F) ppm that are attributed to the enol- and keto-forms of acetylacetone (Figure 2). In addition,
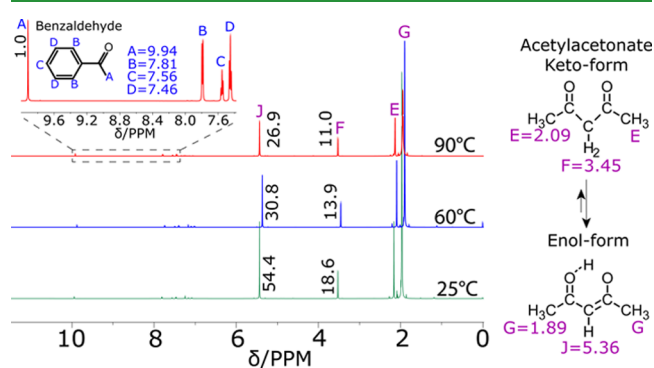

Figure 2. ^{1}H NMR spectra of substances removed from the reaction mixture during degassing at three different temperatures. ^{1}H NMR spectra of substances collected in the cold trap after degassing the synthesis mixture for 1 h at different temperatures and a 30 μbar pressure. The inset is a magnification of the aromatic region. All spectra were recorded at 600 MHz on compounds dissolved in CDCl$_3$. The integrals are written on the spectra.

four minor peaks between 7.46 and 9.94 ppm are observed in the aromatic region of the spectra, which can be assigned to benzaldehyde (BA) (inset of Figure 2). Therefore, the compounds, which were evacuated from the reaction mixture during the degassing process, contain metal coordinating acetylacetonate ligands as a major fraction and a trace amount of BA. The total volume extracted from the cold trap V_t increased from 150 to 250 and 450 μL as the degassing temperature increases from 25 to 60 and 90 °C, respectively. The fraction of acetylacetonate in V_t is given by $\frac{I_{sum}}{1 + I_{sum}}$ and was >96% for all conditions, with I_{sum} being the sum of the integrals

Table 1. Morphological, Structural, and Magnetic Properties of the Three Synthesized Samples[a]

name	L_{ma}	σ_{ma}	x_{ICP}[b]	x_{XRD}[c]	a[c]	$u(O_{32e})$	R_{Bragg}	χ_{global}^2	M_R	H_C
N90	24.1(0.2)	1.6	0.37	0.25−0.35	8.407	0.2519(4)	3.95	1.36	0.02	4.16(0.13)
N60	60.6(1.3)	4.4	0.37	0.25−0.35	8.400	0.2537(4)	2.06	1.74	0.10	9.13(0.08)
N25	96.9(0.5)	4.3	0.37	0.25−0.35	8.409	0.2530(4)	6.34	2.78	0.22	8.15(0.14)

[a]Sample name, mean lateral size of the major particle fraction L_{ma} (nm), standard deviation of Gaussian peaks fitted to size histograms σ_{ma}, zinc doping level x from ICP-AES (x_{ICP}) and XRD (x_{XRD}) analyses, particle lattice constant a (Å), Wyckoff atomic position of oxygen $u(O_{32e})$, R_{Bragg}, χ_{global}^2, reduced remanent magnetization $M_R = M_r/M_s$, and coercive field H_C (mT) derived from TEM, Rietveld analyses, and magnetization measurements. [b]Standard errors of a and x_{ICP} are very small and therefore not given. Errors of M_R are less than 1%. Numbers given in parentheses are standard errors of the mean. [c]Amount of iron per unit cell holds $3 - x$.

of J (1H) and $\frac{1}{2} \times$ F (2H) peaks at 5.36 and 3.45 ppm. The amounts of extracted acetylacetonate are 89, 49, and 29% of the amount initially present (1 mmol of Fe(III) acetylacetonate and 1 mmol of Zn(II) acetylacetonate, corresponding to 495 μL total) after degassing at 90, 60, and 25 °C, respectively. Therefore, there is a significant difference between the abundance of acetylacetonate in the reaction mixture during the nucleation and growth depending upon the degassing temperature.

To determine the decomposition pathway of the precursor and the role of acetylacetonate ligands on particle formation, we probed the species which are formed at different temperatures and reflux times by attenuated total reflection-Fourier transform infrared (ATR-FTIR) spectroscopy. The FTIR spectra show several absorption bands (Figure S3), which mostly remain unchanged during the entire reaction and likely stem from DBE and oleic acid. In contrast, several bands in the region of 1500 to 1800 cm^{-1} change drastically during the synthesis reaction (Figure 3a−c). The bands at 1717 and 1703 cm^{-1} can be assigned to the carbonyl C=O stretching vibration. These bands resemble the characteristic double bond of the carbonyl in the acetylacetonate.[47] We found that the temporal evolution of the carbonyl bands strongly depends on the degassing temperature. In the N90 sample, the acetylacetone ligands lose their characteristic double band feature already at 260 °C (Figure 3a). At this temperature, an additional broad band at 1693 cm^{-1} appears, which becomes more pronounced up to the reflux temperature and then retreats and disappears as the reflux proceeds. The band at 1693 cm^{-1} plausibly originates from a resonant form of acetylacetonate after dissociation from the metal center. We hypothesize that the dissociation of acetylacetonate and formation of monomers coincide with the time at which the third band emerges.

In the N60 sample (Figure 3b), the third band at 1693 cm^{-1} appears later in the reaction time, implying a delayed formation of monomers, compared to the N90 condition. Similar to the N60 sample, the band decreases and eventually disappears as the reaction continues. If the degassing temperature is decreased further to 25 °C, the bands in the spectral regime around 1700 cm^{-1} exhibit a different temporal evolution compared to the higher degassing temperatures. The double bands of the carbonyl at 1703−1717 cm^{-1} retain their shape and mostly decrease in intensity during the synthesis reaction. In addition, no band at 1693 cm^{-1} appears during the reaction. Together, the data indicate an even more delayed monomer formation compared to the higher temperatures (Figure 3c). The evolution of the carbonyl bands for degassing at 25 °C looks as if the acetylacetonate ligands remain bound to metal ions throughout the whole reaction, which might suggest that the acetylacetonate binds to metal ions on the particle surface during nucleation and growth of N25 particles.

To shed light on the effect of the dissociation rate of the acetylacetonate on the particle nucleation and growth mechanism, we performed TEM analysis on aliquots taken at different reflux times. For the N90 sample, no crystallites were formed after 0 min of reflux at 290 °C (Figure S4a). After reacting for 5 min, we observed that a large amount of ≈5 nm semispherical crystallites is formed, suggesting that degassing at 90 °C results in early supersaturation of monomers, leading to a burst nucleation of tiny monodisperse crystallites via LaMer and Dinegar's nucleation model[48] (Figure 4a). By
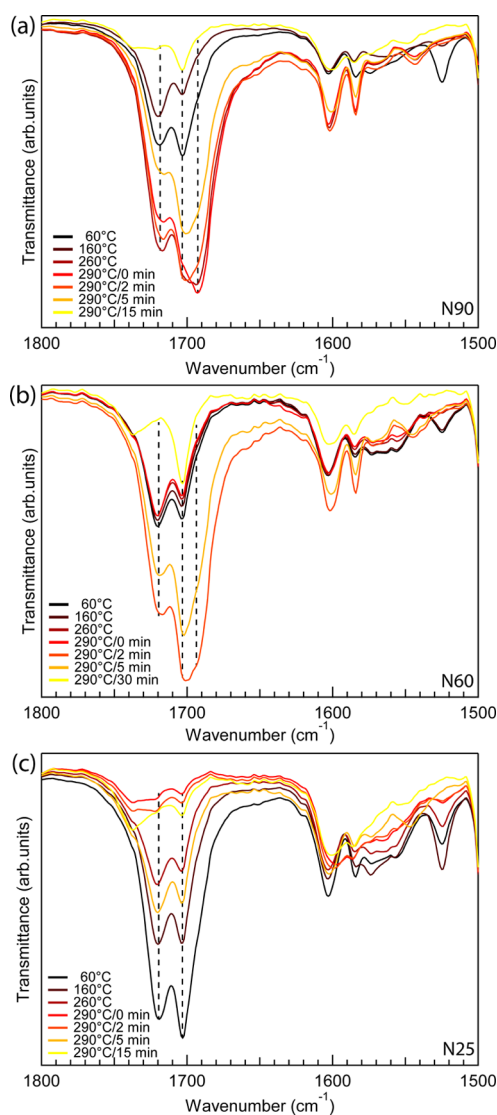
Figure 3. Attenuated total reflection-Fourier transform infrared (ATR-FTIR) spectra of aliquots sampled from the synthesis reaction at different temperatures and reflux times. The temporal evolution of the FTIR spectrum recorded on the whole reaction mixture after degassing at (a) 90 (N90), (b) 60 (N60), and (c) 25 °C (N25). Full spectra are shown in the Supporting Information.

continuing the reaction for 30 min at 290 °C, the crystallites grow to cubes with lateral sizes of 24 nm, through a thermodynamically driven shape evolution.[49] The particle surface area A grows approximately linearly with reflux time t (Figure 4b), suggesting that the growth of the N90 nanocubes is governed by a reaction-controlled growth mechanism.[50] The burst nucleation mechanism leads to a rapid consumption of monomers, which sets a typical upper particle size limit of ≈30 nm.

When the reaction is degassed at 60 °C, cubic-like assembled structures with mean lateral sizes of ≈27 nm made of irregular crystallites are formed after refluxing for 5 min (red arrow in Figure 4c, right side TEM image), instead of burst nucleation of spherical crystallites. Note that no crystalline particles were formed after 2 min of reflux, as examined by TEM (Figure S4b). The cubic structures nearly double their size by continuing the reaction for another 10 min, yet having a nonuniform structure (red arrow in Figure
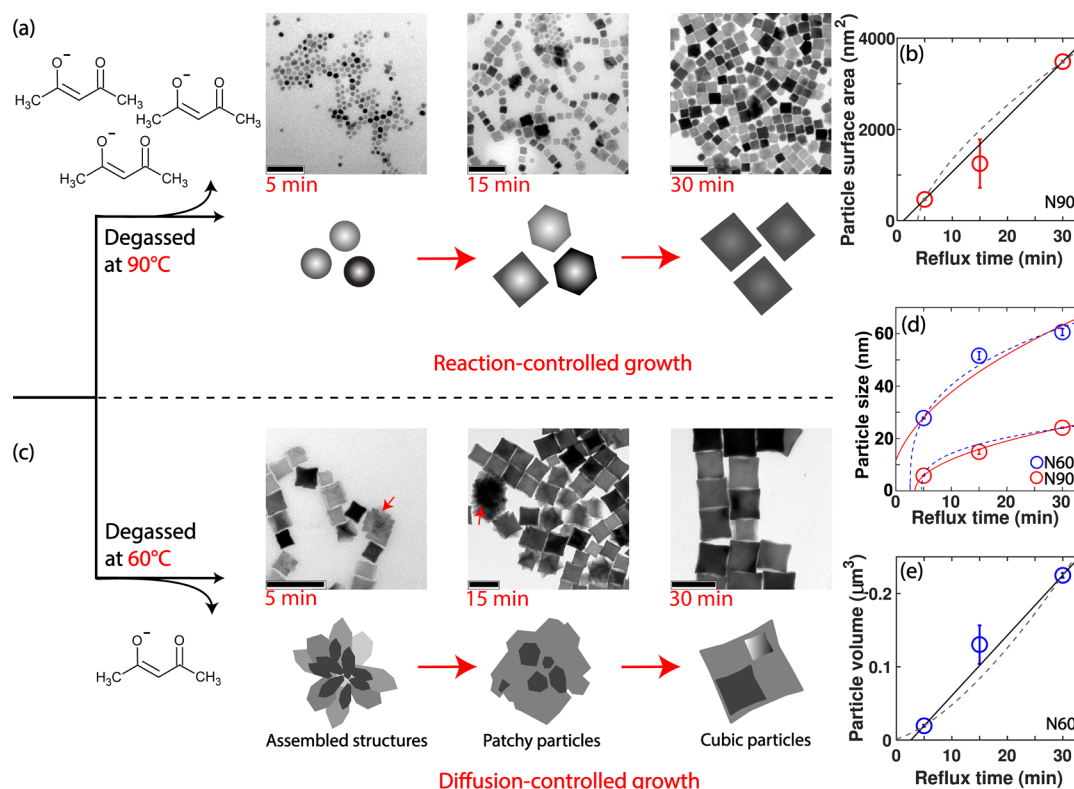
Figure 4. TEM analysis of particles synthesized at different degassing temperatures reveals competing particle morphologies and growth pathways. (a) Temporal evolution of the particle morphology during reflux at 290 °C for up to 30 min and (b) particle surface area vs reflux time at 290 °C for the synthesis reaction degassed at 90 °C. Symbols and error bars in panel (b) are the mean and standard deviation of the area distributions obtained from analysis of TEM images at the corresponding time points, respectively. The data are well described by the reaction-controlled growth model where area ∝ time (solid line; reduced $\chi^2 = 0.64$) and deviate from the diffusion-controlled model where volume ∝ time (dashed line; reduced $\chi^2 = 1.91$). (c) Temporal evolution of the particle morphology during reflux at 290 °C for up to 30 min for the synthesis reaction degassed at 60 °C. (d) Particle size vs reflux time for N90 and N60 samples. Solid red and dashed blue lines are fits to size ∝ $t^{(1/2)}$ and size ∝ $t^{(1/3)}$, representing the reaction- and diffusion-controlled models, respectively. (e) Particle volume vs reflux time at 290 °C for the synthesis reaction degassed at 60 °C. Symbols and error bars are the mean and standard deviation of the volume distributions obtained from analysis of TEM images at the corresponding time points, respectively. The data are well described by the diffusion-controlled growth model (solid line; reduced $\chi^2 = 1.19$) and deviate from the reaction-controlled model (dashed line; reduced $\chi^2 = 3.15$). Symbols are larger than error bars for some data points in panels (b) and (d). The TEM scale bar is 100 nm.

4c, middle TEM micrograph). As the growth progresses further, the structures transform to well-defined nanocubes with a side length of ≈60 nm, much larger than the nanocubes grown after degassing at 90 °C (Figure 4d). For the sample degassed at 60 °C, the particle volume V increases approximately linearly with reflux time t (Figure 4e), indicating that a diffusion-controlled growth mechanism is dominant.[50] Diffusion-controlled growth is characterized by slow diffusion of monomers toward the particle surface and their quick interaction/accumulation at the surface.

From NMR and FTIR analyses, we found that low-temperature degassing results in a higher abundance of the acetylacetonate during the nucleation and growth. We hypothesize that the acetylacetonate ligand outcompetes oleic acid in binding to primary crystallites owing to its small size and bidentate binding chemistry. Plausibly, the acetylacetonate ligands increase surface activity of primary crystallites, resulting in the dominance of the diffusion-controlled growth model in the N60 sample (Figure 4c). In addition, the acetylacetonate ligands appear to enhance the mobility of the smaller crystallites, facilitating their accumulation into larger assembled structures that ultimately rearrange themselves into coherent cubes. In contrast, degassing at high temperature

dissociates most of the acetylacetonate, likely resulting in an earlier formation of monomers, supersaturation, and burst nucleation. The lack of acetylacetonate ligand combined with an abundance of oleic acid might result in a lower surface activity of primary crystallites, which would explain the observation of a reaction-controlled growth.

Since the particle crystal structure and Zn^{2+} distribution in the lattice directly influence the magnetic properties, we next performed powder X-ray diffraction (XRD) analysis. The XRD patterns show sharp and intense reflections, confirming high crystallinity of the synthesized particles (Figure 5a–c). The reflection positions and relative intensities can be indexed to a single cubic spinel phase for all three samples. The major reflections are labeled in Figure 5a. No unassigned reflection remains, implying that the insertion of Zn^{2+} into the lattice did not result in the formation of other crystalline phases. The XRD patterns were analyzed by quantitative Rietveld pattern refinement to obtain the crystal lattice constant a, the site occupancy of Fe^{3+} and Zn^{2+} in tetrahedral sites, and the Wyckoff atomic position of oxygen $u(O_{32e})$ using the Fullprof Suite software.[51] The patterns were refined assuming an inverse spinel crystal structure with the $Fd\bar{3}m$ space group. The
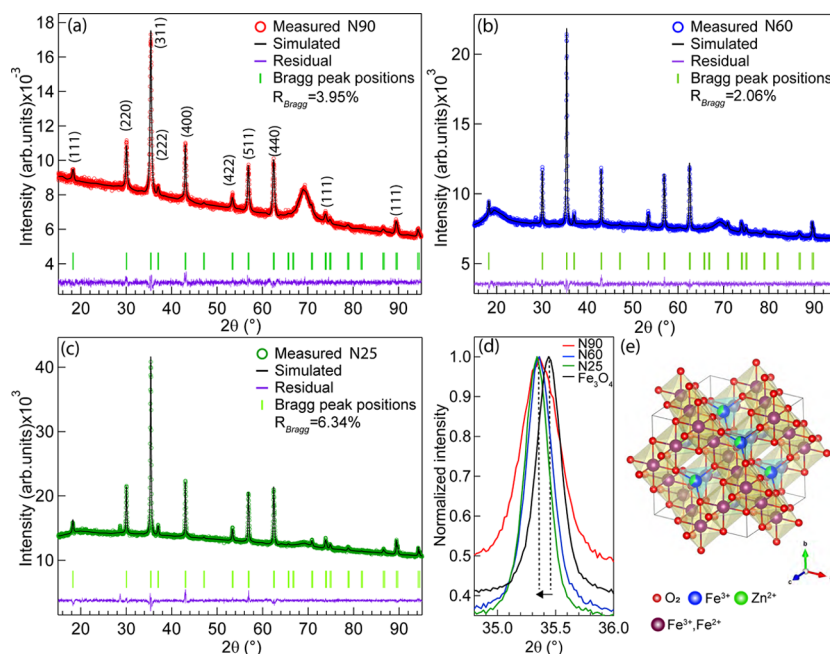
Figure 5. X-ray diffraction patterns and Rietveld pattern refinement analyses. Powder X-ray diffraction patterns of (a) N90, (b) N60, and (c) N25 samples. The simulated patterns based on the Rietveld analysis of XRD patterns, the Bragg peak positions, and the fit residual are coplotted together with the measured patterns. The broad peak at $2\theta = 69°$ is a reflection from the silicon wafer. (d) Comparison between the peak position of the (311) reflection in different samples compared to 200 nm Fe_3O_4 nanocubes synthesized via an otherwise identical synthesis procedure without zinc. (e) Cubic lattice structure of $Zn_{0.37}Fe_{2.63}O_4$ representing Fe^{3+} and Zn^{2+} cations sharing tetrahedral sites and Fe^{3+} and Fe^{2+} occupying octahedral sites.
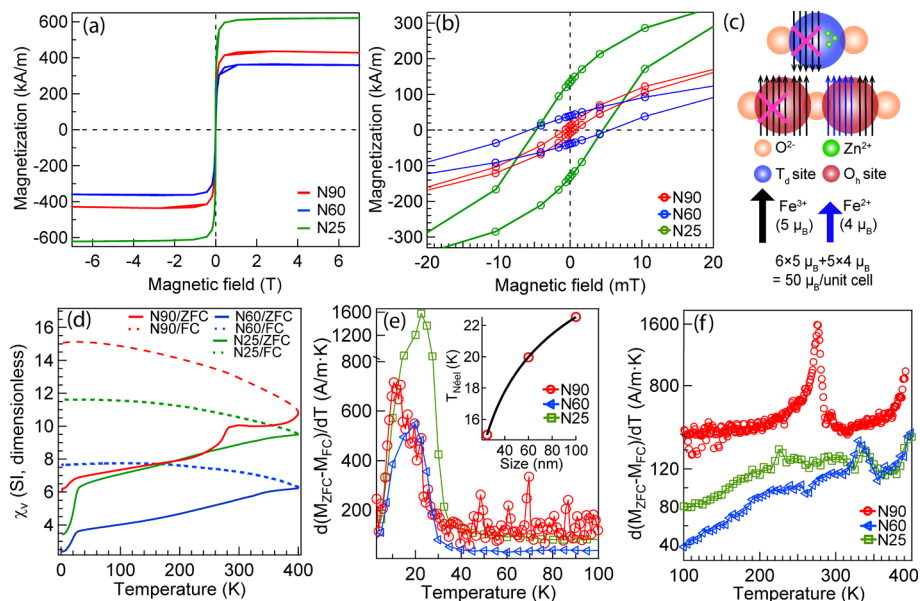

Figure 6. Magnetization as a function of magnetic field and temperature-dependent susceptibility measured in a direct current (DC) measurement mode. (a,b) Volume magnetization vs magnetic field $M-H$ loops of all three samples measured at room temperature. The reported magnetization values are normalized to the total mass of zinc ferrite nanoparticles assuming a density of 5.25 g/cm³. (c) Magnetic spins' configuration of a ferrimagnetic $Zn_{0.375}Fe_{2.625}O_4$ with an inverse spinel crystal structure for a unit cell. (d) Volume DC susceptibility measured at 10 mT magnetic fields in zero-field-cooled (ZFC) (solid lines) and field-cooled (FC) (dashed lines) modes vs temperature. (e) $d(M_{ZFC} - M_{FC})/dT$ vs T plotted from 2 to 100 K; the inset shows the dependence of the Néel transition temperature on the particle size. The solid line is a guide to the eye. (f) $d(M_{ZFC} - M_{FC})/dT$ vs T plotted from 100 to 400 K; the solid line is a Gaussian fit.

refinement sequence of the fit parameters is described in detail in the Supporting Information.

The best fits to the XRD patterns were obtained by considering larger lattice constants a than magnetite nanocubes, that is, 8.39 Å,[15] synthesized using an otherwise

identical protocol without adding zinc (Table 1). The expansion of a indicates a successful insertion of Zn^{2+} into the spinel lattice, which is qualitatively manifested in a shift in the XRD peak positions (Figure 5d). For all three samples, the atom site occupancies of Zn^{2+} and Fe^{3+} in the tetrahedral T_d

sites vary between 0.25 and 0.35 and 0.75 and 0.65, respectively, as deduced from the Rietveld analyses. The goodness of the Rietveld refinement, determined by R_{Bragg} and χ_{global}^2, does not change significantly for values within these ranges (Table 1). The uncertainty in the atom site occupancies may originate from similar scattering factor of zinc and iron. However, we note that the goodness of fit did worsen by inserting Zn^{2+} in the octahedral sites O_h. The insertion of Zn^{2+} into the Fe_3O_4 lattice leads to the substitution of Fe^{3+} in T_d with Zn^{2+} owing to higher affinity of zinc to these crystalline sites. As a result, Fe^{3+} cations migrate to O_h sites. The Wyckoff atomic position of oxygen $u(O_{32e})$ falls within the expected range for a minimally distorted face-centered cubic (fcc) lattice, which is 0.255−0.260.[52] The most plausible formula unit of the synthesized nanocubes is therefore $(Zn^{2+}Fe^{3+})_x^{T_d}(Fe^{3+}Fe^{2+})_{3-x}^{T_d,O_h}O_4$. The zinc concentration estimated from the XRD analysis was on average 20% smaller than that of ICP-AES elemental analysis, still agreeing within error (Table 1), which plausibly attributes to the fact that, in an ICP analysis, all existing zinc ions are measured regardless of being embedded in the lattice or being dissolved in the solution upon shelf storage.

To determine how the Zn^{2+} substitution influences the particle magnetization, we recorded field- and temperature-dependent magnetization data. The saturation magnetization M_s values, here estimated from magnetization $M-H$ curves, are 430, 360, and 620 kA/m for N90, N60, and N25 samples, respectively (Figure 6a). These values exceed the typical values reported for Fe_3O_4 nanoparticles in the literature, varying from 300 to 450 kA/m,[15,53] indicating uncompensated Fe^{3+} in O_h sites and effective insertion of Zn^{2+} in T_d sites (Figure 6c). The N25 nanocubes show an extraordinarily high room-temperature M_s, which corresponds to 188 emu/g_{Fe}, assuming $\rho = 5.25$ g/cm^3. M_s of the N25 nanocubes is ~1.5 times higher than the bulk magnetization of magnetite, which is 124 emu/g_{Fe} (465 kA/m).[40] Given the net magnetic moment of a unit cell of a stoichiometric magnetite of $32\mu_B$, the net magnetic moment of N25 is $48.5\mu_B$ per unit cell (Figure 6c). The estimated magnetic moment corresponds to a replacement of ≈ 2.8 Fe^{3+} ions in T_d sites with Zn^{2+}, corresponding to an ≈ 0.36 Zn^{2+} occupancy, given that the maximum number of ions per unit cell in T_d sites is 8, in excellent agreement with the values determined from XRD and ICP. These ≈ 100 nm N25 nanocubes have an average magnetic moment $\bar{m}$ of 3.56×10^{-16} A m^2 as extracted from the analysis of the $M-H$ curve. Applying 100 mT rotating magnetic fields, these particles can exert up to 3.56×10^4 pN nm magnetic torque, well suited to study dynamics of rotary molecular motors like bacterial flagellar motors of *Escherichia coli* (*E. coli*) bacteria in a single-molecule magnetic tweezers setup.[18,54,55] The generated torque is large enough to stall the flagellar motors of *E. coli* (the stall torque is ≈ 2000 pN nm),[56] a prerequisite to have full control over their rotation dynamics. Therefore, in particular, the large N25 nanocubes are promising candidates for single-molecule magnetic torque tweezers assays.

The inclusion of Zn^{2+} leads to a smaller improvement in M_s for N90 and N60 samples than for N25, yet their M_s values of 130 and 110 emu/g_{Fe} (A m^2/kg$_{Fe}$), respectively, are larger than those reported for 21 nm (<80 A m^2/kg$_{Fe}$),[39] 19 nm (<80 emu/g),[15] and 25 nm (<110 emu/g_{Fe}) iron oxide nanoparticles.[40] Generally, the literature agrees well on maximizing M_s of magnetite by a 0.4−0.5 Zn^{2+} substitution into the lattice.

However, most M_s values reported so far are below what is nominally expected for this amount of substitution[42−44,46,57] (see the scheme in Figure 6c). It has recently been shown that a 0.4 Zn^{2+} insertion into 8 nm zinc cobalt ferrite particles causes weakening of the magnetic exchange coupling J between ions in T_d and O_h sites.[45] A weaker magnetic coupling together with surface and core spin canting,[58] often present in nanosized magnetic particles, can account for a reduced M_s measured for the N90 and N60 samples compared to the N25 particles.

The coercive fields H_C of N90, N60, and N25 samples are 4.16, 9.13, and 8.15 mT (Figure 6b), respectively, suggesting a relatively soft magnetic behavior (Table 1). Interestingly, H_C decreases as the size increases from 60 to 100 nm, which indicates a transition from single-domain to multidomain regime within this size range.

All three samples reveal an abrupt rise in DC volume susceptibility χ_v measured in zero-field-cooled (ZFC) mode with increasing temperature in the regime below 25 K (Figure 6d). At temperatures above 25 K, the ZFC curves rise gradually up to 400 K, and except N90 nanocubes, no other sample reaches a maximum in the temperature regime probed. It is well known that the Verwey transition in magnetite $Fe_{3-\delta}O_4$ vanishes even by a minimal iron deficiency $\delta = 0.06$ or by doping zinc into the lattice.[16,46] The absence of a well-defined transition, particle−particle interactions,[59] and particle size and magnetic energy barrier KV_m distributions can account for a gradual rise of χ_v curves to high temperatures.[60] Plotting $d(M_{ZFC} - M_{FC})/dT$ versus temperature T, all three samples show a sharp transition peak between 15 and 24 K (Figure 6e), shifting to higher temperatures with particle size. The transition could originate from both antiferromagnetic Néel transition T_N and geometrical-frustration due to finite size effects,[61] yet its exact origin is controversial. Similar to our observation, a size-dependent Néel transition was reported in $MnFe_2O_4$ and NiO nanocrystals[62,63] and was related to finite size effects. The T_N versus D data (inset of Figure 6e), however, cannot be fitted to the Binder finite-scaling[64] with parameters in a physically plausible range. The poor fit of the Binder model might partially stem from a difference between T_N(bulk) of our particle composition and that of $ZnFe_2O_4$, that is, 10 K.[61] Unfortunately, the information on the bulk-like behavior of our particle composition is nonexistent, making further discussion on the size-dependent behavior speculative. The higher T_N of the N25 particles can also be partially attributed to a high degree of Zn^{2+} inversion in the lattice.[62]

A highly relevant transition in magnetic nanoparticles for biological applications is the superparamagnetic (SPM) blocking temperature, above which the particles possess no spontaneous magnetization. Like for the low-temperature transition, the SPM blocking temperature T_B of nanoparticles coincides well with the inflection point of the ZFC curve.[22,60] To evaluate this transition, we plotted the differential curves between 100 and 400 K in a separate panel (Figure 6f). The N90 sample shows a narrow SPM transition peak with a mean T_B located at 275 K, indicating that they are superparamagnetic at room temperature. With the superconducting quantum interference device (SQUID) measurement time $\tau_m = 100$ s, assuming an inverse attempt frequency $\tau_0 = 10^{-9}$ s, and Néel−Brownian relaxation behavior for the particles, the magneto-crystalline anisotropy constant K can be estimated from

$$KV_m = 25k_BT_B \qquad (1)$$

in which V_m is the magnetic volume of a single particle and k_B is the Boltzmann constant. We find $K = 6.8$ kJ/m^3 for the 24 nm N90 nanocubes, well below the values reported for bulk-like magnetite in the range of 11−13 kJ/m^3,[37] suggesting that, for our N90 cubes, Néel relaxation is the dominant mechanism. The combination of high M_s and low K in our 24 nm particles makes them promising candidates for intracellular magnetic hyperthermia-assisted drug delivery and cancer therapy, for which particles with large K that mainly relax via the Brownian relaxation mechanism are not suitable due to a highly viscous cellular environment.[65] The other two samples show no sign of the SPM transition up to 400 K, which is expected for the larger particle sizes. In contrast to 24 nm nanocubes, having a ferromagnetic magnetization component in the larger particles is advantageous for exerting large magnetic torque on molecular rotary machines of interest.

We found from ^{1}H NMR spectra recorded on the reaction mixtures at the end of synthesis that a significant amount of benzaldehyde (BA) is formed during the reaction, in particular after degassing at 90 °C, likely due to oxidation of DBE by exposed metal centers (Figure S5, further discussions are given in the Supporting Information). Interestingly, adding 200 μL of reagent-grade BA to the N25 sample synthesis reaction after degassing increases the final particle size for about 15 nm (Figure S6). These observations suggest that, while in our synthesis reactions the acetylacetonate content is the decisive parameter in defining the final particle size, changes in the equilibrium of coordinating ligands can further increase the particle size.

CONCLUSIONS

In summary, we have demonstrated a very significant influence of the reaction degassing temperature on the kinetics of nucleation and growth of zinc ferrite nanocubes synthesized via thermal decomposition of metal acetylacetonates. We have shown that the particle size can be tuned from 25 to 100 nm simply by reducing the pretreating degassing temperature. We have demonstrated that, when the reaction is degassed at 90 °C, a major fraction of the acetylacetone ligands dissociates from metal ions and leaves the reaction vessel, leading to an early nucleation of crystallites, which then follow a reaction-controlled growth pathway. Instead, by degassing at 25 °C, the acetylacetone ligands remain largely associated with metal ions up to high temperatures, resulting in a late decomposition of the precursor. The consequent delayed nucleation and high content of acetylacetone ligands trigger the formation of assembled structures made of small crystallites, which eventually rapidly grow to large nanocubes following a diffusion-controlled growth mechanism. Our synthetic protocol narrows the complex parameter space of thermal decomposition to a single physical parameter. From a technological point of view, our procedure simplifies size-controlled synthesis of highly magnetic nanoparticles over a wide size range. The smaller nanocubes are promising candidates for intracellular magnetic hyperthermia cancer therapy and drug delivery as well as magnetic particle imaging by offering a combination of high saturation magnetization and low magnetic anisotropy constant. In contrast, the larger zinc ferrite nanocubes with their ferromagnetic magnetization component and larger magnetic moments and torques are of great interest for manipulation of molecular rotary machines, for example, bacterial flagellar motors in single-molecule magnetic tweezers. We envisage that the approach developed here can potentially be extended to size-controlled synthesis of other magnetic materials such as iron oxide, manganese-doped zinc ferrite, and cobalt ferrite nanoparticles.

ASSOCIATED CONTENT

ⓢ Supporting Information

The Supporting Information is available free of charge at https://pubs.acs.org/doi/10.1021/acsami.9b17714.

Heating profiles for particle synthesis reactions, Rietveld XRD pattern refinement scheme and results, ^{1}H NMR spectra and further discussion on ^{1}H NMR results, ATR-FTIR spectra, and TEM images (PDF)

AUTHOR INFORMATION

Corresponding Authors

*E-mail: lak.aidin@physik.uni-muenchen.de (A.L.).
*E-mail: jan.lipfert@lmu.de (J.L.).

ORCID ⓘ

Aidin Lak: 0000-0003-1219-2866
Peter Müller-Buschbaum: 0000-0002-9566-6088
Jan Lipfert: 0000-0003-3613-7896

Notes

The authors declare no competing financial interest.

REFERENCES

(1) Pankhurst, Q. A.; Connolly, J.; Jones, S. K.; Dobson, J. Magnetic Nanoparticles: Synthesis, Protection, Functionalization, and Application. *J. Phys. D: Appl. Phys.* **2003**, *36*, R167−R181.

(2) Jeong, U.; Teng, X.; Wang, Y.; Yang, H.; Xia, Y. Superparamagnetic Colloids: Controlled Synthesis and Niche Applications. *Adv. Mater.* **2007**, *19*, 33−60.

(3) Na, H. B.; Song, I. C.; Hyeon, T. Inorganic Nanoparticles for MRI Contrast Agents. *Adv. Mater.* **2009**, *21*, 2133−2148.

(4) Krishnan, K. M. Biomedical Nanomagnetics: A Spin Through Possibilities in Imaging, Diagnostics, and Therapy. *IEEE Trans. Magn.* **2010**, *46*, 2523−2558.

(5) Ho, D.; Sun, X.; Sun, S. Monodisperse Magnetic Nanoparticles for Theranostic Applications. *Acc. Chem. Res.* **2011**, *44*, 875−882.

(6) Gleich, B.; Weizenecker, J. Tomographic Imaging Using the Nonlinear Response of Magnetic Particles. *Nature* **2005**, *435*, 1214−1217.

(7) Hyeon, T. Chemical Synthesis of Magnetic Nanoparticles. *Chem. Commun.* **2003**, 927−934.

(8) Sun, S.; Zeng, H. Size-controlled Synthesis of Magnetite Nanoparticles. *J. Am. Chem. Soc.* **2002**, *124*, 8204−8205.

(9) Park, J.; An, K.; Hwang, Y.; Park, J. G.; Hon, H. J.; Kim, J. Y.; Park, J. H.; Hwang, N. M.; Hyeon, T. Ultra-large-scale Syntheses of Monodisperse Nanocrystals. *Nat. Mater.* **2004**, *3*, 891−895.

(10) Hyeon, T.; Lee, S. S.; Park, J.; Chung, Y.; Na, H. B. Synthesis of Highly Crystalline and Monodisperse Maghemite Nanocrystallites without a Size-Selection Process. *J. Am. Chem. Soc.* **2001**, *123*, 12798−12801.

(11) Redl, F. X.; Black, C. T.; Papaefthymiou, G. C.; Sandstrom, R. L.; Yin, M.; Zeng, H.; Murray, C. B.; O'Brien, S. P. Magnetic, Electronic, and Structural Characterization of Nonstoichiometric Iron Oxides at the Nanoscale. *J. Am. Chem. Soc.* **2004**, *126*, 14583−14599.

(12) Kovalenko, M. V.; Bodnarchuk, M. I.; Lechner, R. T.; Hesser, G.; Schäffler, F.; Heiss, W. Fatty Acid Salts as Stabilizers in Size- and Shape-Controlled Nanocrystal Synthesis: The Case of Inverse Spinel Iron Oxide. *J. Am. Chem. Soc.* **2007**, *129*, 6352−6353.

(13) Kim, D.; Lee, N.; Park, M.; Kim, B. H.; An, K.; Hyeon, T. Synthesis of Uniform Ferrimagnetic Magnetite Nanocubes. *J. Am. Chem. Soc.* **2009**, *131*, 454−455.

(14) Guardia, P.; Pérez-Juste, J.; Labarta, A.; Batlle, X.; Liz-Marzán, L. M. Heating Rate Inuence on the Synthesis of Iron Oxide Nanoparticles: the Case of Decanoic Acid. *Chem. Commun.* **2010**, *46*, 6108−6110.

(15) Guardia, P.; Di Corato, R.; Lartigue, L.; Wilhelm, C.; Espinosa, A.; Garcia-Hernandez, M.; Gazeau, F.; Manna, L.; Pellegrino, T. Water-soluble Iron Oxide Nanocubes with High Values of Specific Absorption Rate for Cancer Cell Hyperthermia Treatment. *ACS Nano* **2012**, *6*, 3080−3091.

(16) Lak, A.; Cassani, M.; Mai, B. T.; Winckelmans, N.; Cabrera, D.; Sadrollahi, E.; Marras, S.; Remmer, H.; Fiorito, S.; Cremades-Jimeno, L.; Litterst, F. J.; Ludwig, F.; Manna, L.; Teran, F. J.; Bals, S.; Pellegrino, T. Fe^{2+} Deficiencies, FeO Subdomains, and Structural Defects Favor Magnetic Hyperthermia Performance of Iron Oxide Nanocubes into Intracellular Environment. *Nano Lett.* **2018**, *18*, 6856−6866.

(17) Lipfert, J.; Kerssemakers, J. W.; Jager, T.; Dekker, N. H. Magnetic Torque Tweezers : Measuring Torsional Sti_ness in DNA and RecA-DNA Filaments. *Nat. Methods* **2010**, *7*, 2875−2980.

(18) Lipfert, J.; Van Oene, M. M.; Lee, M.; Pedaci, F.; Dekker, N. H. Torque Spectroscopy for the Study of Rotary Motion in Biological Systems. *Chem. Rev.* **2015**, *115*, 1449−1474.

(19) Moerland, C. P.; van IJzendoorn, L. J.; Prins, M. W. J. Rotating Magnetic Particles for Lab-on-Chip Applications - a Comprehensive Review. *Lab Chip* **2019**, *19*, 919−933.

(20) Kim, J.-W.; Jeong, H.-K.; Southard, K. M.; Jun, Y.-W.; Cheon, J. Magnetic Nanotweezers for Interrogating Biological Processes in Space and Time. *Acc. Chem. Res.* **2018**, *51*, 839−849.

(21) Shavel, A.; Rodríguez-González, B.; Spasova, M.; Farle, M.; Liz-Marzán, L. M. Synthesis and Characterization of Iron/Iron Oxide Core/Shell Nanocubes. *Adv. Funct. Mater.* **2007**, *17*, 3870−3876.

(22) Pichon, B. P.; Gerber, O.; Lefevre, C.; Florea, I.; Fleutot, S.; Baaziz, W.; Pauly, M.; Ohlmann, M.; Ulhaq, C.; Ersen, O.; Pierron-Bohnes, V.; Panissod, P.; Drillon, M.; Begin-Colin, S. Microstructural and Magnetic Investigations of Wüstite-Spinel Core-Shell Cubic-Shaped Nanoparticles. *Chem. Mater.* **2011**, *23*, 2886−2900.

(23) Lee, N.; Choi, Y.; Lee, Y.; Park, M.; Moon, W. K.; Choi, S. H.; Hyeon, T. Water-Dispersible Ferrimagnetic Iron Oxide Nanocubes with Extremely High r_2 Relaxivity for Highly Sensitive in Vivo MRI of Tumors. *Nano Lett.* **2012**, *12*, 3127−3131.

(24) Wetterskog, E.; Tai, C.-W.; Grins, J.; Bergström, L.; Salazar-Alvarez, G. Anomalous Magnetic Properties of Nanoparticles Arising from Defect Structures: Topotaxial Oxidation of $Fe_{1-x}O|Fe_{3-\delta}O_4$ CorejShell Nanocubes to Single-Phase Particles. *ACS Nano* **2013**, *7*, 7132−7144.

(25) Walter, A.; Billotey, C.; Garofalo, A.; Ulhaq-Bouillet, C.; Lefévre, C.; Taleb, J.; Laurent, S.; Elst, L. V.; Muller, R. N.; Lartigue, L.; Gazeau, F.; Felder-Flesch, D.; Begin-Colin, S. Mastering the Shape and Composition of Dendronized Iron Oxide Nanoparticles To Tailor Magnetic Resonance Imaging and Hyperthermia. *Chem. Mater.* **2014**, *26*, 5252−5264.

(26) Feld, A.; Weimer, A.; Kornowski, A.; Winckelmans, N.; Merkl, J.-P.; Kloust, H.; Zierold, R.; Schmidtke, C.; Schotten, T.; Riedner,

M.; Bals, S.; Weller, H. Chemistry of Shape-Controlled Iron Oxide Nanocrystal Formation. *ACS Nano* **2019**, *13*, 152−162.

(27) Cotin, G.; Kiefer, C.; Perton, F.; Ihiawakrim, D.; Blanco-Andujar, C.; Moldovan, S.; Lefevre, C.; Ersen, O.; Pichon, B.; Mertz, D.; Bégin-Colin, S. Unravelling the Thermal Decomposition Parameters for The Synthesis of Anisotropic Iron Oxide Nanoparticles. *Nanomaterials* **2018**, *8*, 881.

(28) Bronstein, L. M.; Atkinson, J. E.; Malyutin, A. G.; Kidwai, F.; Stein, B. D.; Morgan, D. G.; Perry, J. M.; Karty, J. a. Nanoparticles by Decomposition of Long Chain Iron Carboxylates: From Spheres to Stars and Cubes. *Langmuir* **2011**, *27*, 3044−3050.

(29) Zhao, Z.; Zhou, Z.; Bao, J.; Wang, Z.; Hu, J.; Chi, X.; Ni, K.; Wang, R.; Chen, X.; Chen, Z.; Gao, J. Octapod Iron Oxide Nanoparticles as High-performance T2 Contrast Agents for Magnetic Resonance Imaging. *Nat. Commun.* **2013**, *4*, 1−7.

(30) Gavilán, H.; Kowalski, A.; Heinke, D.; Sugunan, A.; Sommertune, J.; Var_on, M.; Bogart, L. K.; Posth, O.; Zeng, L.; González-Alonso, D.; Balceris, C.; Fock, J.; Wetterskog, E.; Frandsen, C.; Gehrke, N.; Grüttner, C.; Fornara, A.; Ludwig, F.; Veintemillas-Verdaguer, S.; Johansson, C.; Morales, M. P. Colloidal Flower-Shaped Iron Oxide Nanoparticles: Synthesis Strategies and Coatings. *Part. Part. Syst. Charact.* **2017**, *34*, 1700094.

(31) Salazar-Alvarez, G.; Qin, J.; Šepelák, V.; Bergmann, I.; Vasilakaki, M.; Trohidou, K. N.; Ardisson, J. D.; Macedo, W. A. A.; Mikhaylova, M.; Muhammed, M.; Baró, M. D.; Nogués, J. Cubic versus Spherical Magnetic Nanoparticles: The Role of Surface Anisotropy. *J. Am. Chem. Soc.* **2008**, *130*, 13234−13239.

(32) Muro-Cruces, J.; Roca, A. G.; López-Ortega, A.; Fantechi, E.; del Pozo-Bueno, D.; Estradé, S.; Peiró, F.; Sepúlveda, B.; Pineider, F.; Sangregorio, C.; Nogues, J. Precise Size Control of the Growth of Fe_3O_4 Nanocubes over a Wide Size Range Using a Rationally Designed One-Pot Synthesis. *ACS Nano* **2019**, *13*, 7716−7728.

(33) López-Ortega, A.; Lottini, E.; Fernández, C. d. J.; Sangregorio, C. Exploring the Magnetic Properties of Cobalt-Ferrite Nanoparticles for the Development of a Rare-Earth-Free Permanent Magnet. *Chem. Mater.* **2015**, *27*, 4048−4056.

(34) Kwon, S. G.; Piao, Y.; Park, J.; Angappane, S.; Jo, Y.; Hwang, N.-m.; Park, J.-g.; Hyeon, T. Kinetics of Monodisperse Iron Oxide Nanocrystal Formation by "Heating-Up" Process. *J. Am. Chem. Soc.* **2007**, *129*, 12571−12584.

(35) Lee, N.; Kim, H.; Choi, S. H.; Park, M.; Kim, D.; Kim, H.-C.; Choi, Y.; Lin, S.; Kim, B. H.; Jung, H. S.; Kim, H.; Park, K. S.; Moon, W. K.; Hyeon, T. Magnetosome-Like Ferrimagnetic Iron Oxide Nanocubes for Highly Sensitive MRI of Single Cells and Transplanted Pancreatic Islets. *Proc. Natl. Acad. Sci. U. S. A.* **2011**, *108*, 2662−2667.

(36) Nemati, Z.; Alonso, J.; Rodrigo, I.; Das, R.; Garaio, E.; García, J. n.; Orue, I.; Phan, M.-H.; Srikanth, H. Improving the Heating Efficiency of Iron Oxide Nanoparticles by Tuning Their Shape and Size. *J. Phys. Chem. C* **2018**, *122*, 2367−2381.

(37) Hufschmid, R.; Arami, H.; Ferguson, R. M.; Gonzales, M.; Teeman, E.; Brush, L. N.; Browning, N. D.; Krishnan, K. M. Synthesis of Phase-Pure and Monodisperse Iron Oxide Nanoparticles by Thermal Decomposition. *Nanoscale* **2015**, *7*, 11142−11154.

(38) Kemp, S. J.; Ferguson, R. M.; Khandhar, A. P.; Krishnan, K. M. Monodisperse Magnetite Nanoparticles with Nearly Ideal Saturation Magnetization. *RSC Adv.* **2016**, *6*, 77452−77464.

(39) Unni, M.; Uhl, A. M.; Savliwala, S.; Savitzky, B. H.; Dhavalikar, R.; Garraud, N.; Arnold, D. P.; Kourkoutis, L. F.; Andrew, J. S.; Rinaldi, C. Thermal Decomposition Synthesis of Iron Oxide Nanoparticles with Diminished Magnetic Dead Layer by Controlled Addition of Oxygen. *ACS Nano* **2017**, *11*, 2284−2303.

(40) Chen, R.; Christiansen, M. G.; Sourakov, A.; Mohr, A.; Matsumoto, Y.; Okada, S.; Jasanoff, A.; Anikeeva, P. High-Perform-ance Ferrite Nanoparticles through Nonaqueous Redox Phase Tuning. *Nano Lett.* **2016**, *16*, 1345−1351.

(41) Jang, J. T.; Nah, H.; Lee, J. H.; Moon, S. H.; Kim, M. G.; Cheon, J. Critical Enhancements of MRI Contrast and Hyperthermic Effects by Dopant-Controlled Magnetic Nanoparticles. *Angew. Chem., Int. Ed.* **2009**, *48*, 1234−1238.

(42) Yang, Y.; Liu, X.; Yang, Y.; Xiao, W.; Li, Z.; Xue, D.; Li, F.; Ding, J. Synthesis of Nonstoichiometric Zinc Ferrite Nanoparticles with Extraordinary Room Temperature Magnetism and their Diverse Applications. *J. Mater. Chem. C* **2013**, *1*, 2875−2885.

(43) Byrne, J. M.; Coker, V. S.; Cespedes, E.; Wincott, P. L.; Vaughan, D. J.; Pattrick, R. A. D.; van der Laan, G.; Arenholz, E.; Tuna, F.; Bencsik, M.; Lloyd, J. R.; Telling, N. D. Biosynthesis of Zinc Substituted Magnetite Nanoparticles with Enhanced Magnetic Properties. *Adv. Funct. Mater.* **2014**, *24*, 2518−2529.

(44) Bauer, L. M.; Situ, S. F.; Griswold, M. A.; Samia, A. C. S. High-Performance Iron Oxide Nanoparticles for Magnetic Particle Imaging-Guided Hyperthermia (hMPI). *Nanoscale* **2016**, *8*, 12162−12169.

(45) Albino, M.; Fantechi, E.; Innocenti, C.; López-Ortega, A.; Bonanni, V.; Campo, G.; Pineider, F.; Gurioli, M.; Arosio, P.; Orlando, T.; Bertoni, G.; de Julián Fernández, C.; Lascialfari, A.; Sangregorio, C. Role of Zn^{2+} Substitution on the Magnetic, Hyperthermic, and Relaxometric Properties of Cobalt Ferrite Nanoparticles. *J. Phys. Chem. C* **2019**, *123*, 6148−6157.

(46) Fontaiña-Troitiño, N.; Ramos-Docampo, M. A.; Testa-Anta, M.; Rodríguez-González, B.; Bañobre-López, M.; Bocher, L.; McKenna, K. P.; Salgueiriño, V. Antiphase Boundaries in Truncated Octahedron-Shaped Zn-Doped Magnetite Nanocrystals. *J. Mater. Chem. C* **2018**, *6*, 12800−12807.

(47) Robert, M. S.; Francis, X. W.; David, J. K. *Spectrometric Identification of Organic Compounds*; seventh ed.; Wiley: Hoboken, NJ, 1981.

(48) LaMer, V. K.; Dinegar, R. H. Theory, Production and Mechanism of Formation of Monodispersed Hydrosols. *J. Am. Chem. Soc.* **1950**, *72*, 4847−4854.

(49) Qiao, L.; Fu, Z.; Li, J.; Ghosen, J.; Zeng, M.; Stebbins, J.; Prasad, P. N.; Swihart, M. T. Standardizing Size- and Shape-Controlled Synthesis of Monodisperse Magnetite Fe_3O_4 Nanocrystals by Identifying and Exploiting Effects of Organic Impurities. *ACS Nano* **2017**, *11*, 6370−6381.

(50) Sarma, R. V. D. D. In *Nanomaterials Chemistry: Recent Developments and New Directions*; Rao, C. N. R., Müller, A.; Cheetham, A. K. Ed.; Wiley-VCH Verlag GmbH & Co. KGaA: Weinheim, 2007; Chapter 4, pp 139−170.

(51) Rodriguez-Carvajal, J. *FullProf Suite*; LLB Saclay & LCSIM: Rennes, France, 2003.

(52) Andersen, H. L.; Saura-Múzquiz, M.; Granados-Miralles, C.; Canévet, E.; Lock, N.; Christensen, M. Crystalline and Magnetic Structure-Property Relationship in Spinel Ferrite Nanoparticles. *Nanoscale* **2018**, *10*, 14902−14914.

(53) Roca, A. G.; Morales, M. P.; O'Grady, K.; Serna, C. J. Structural and Magnetic Properties of Uniform Magnetite Nanoparticles Prepared by High Temperature Decomposition of Organic Precursors. *Nanotechnology* **2006**, *17*, 2783−2788.

(54) Forth, S.; Sheinin, M. Y.; Inman, J.; Wang, M. D. Torque Measurement at the Single-Molecule Level. *Annu. Rev. Biophys.* **2013**, *42*, 583−604.

(55) van Oene, M. M.; Dickinson, L.; Cross, B.; Pedaci, F.; Lipfert, J.; Dekker, N. H. Applying Torque to the Escherichia Coli Flagellar Motor Using Magnetic Tweezers. *Sci. Rep.* **2017**, *7*, 43285.

(56) Mandadapu, K. K.; Nirody, J. A.; Berry, R. M.; Oster, G. Mechanics of Torque Generation in the Bacterial Flagellar Motor. *Proc. Natl. Acad. Sci. U. S. A.* **2015**, *112*, E4381−E4389.

(57) Park, J.; Porter, M. D.; Granger, M. C. Silica Encapsulation of Ferrimagnetic Zinc Ferrite Nanocubes Enabled by Layer-by-Layer Polyelectrolyte Deposition. *Langmuir* **2015**, *31*, 3537−3545.

(58) Morales, M. P.; Serna, C. J.; Bødker, F.; Mørup, S. Spin Canting due to Structural Disorder in Maghemite. *J. Phys. Condens. Matter* **1997**, *9*, 5461−5467.

(59) Lak, A.; Kraken, M.; Ludwig, F.; Kornowski, A.; Eberbeck, D.; Sievers, S.; Litterst, F. J.; Weller, H.; Schilling, M. Size Dependent Structural and Magnetic Properties of FeO-Fe_3O_4 Nanoparticles. *Nanoscale* **2013**, *5*, 12286−12295.

(60) Livesey, K. L.; Ruta, S.; Anderson, N. R.; Baldomir, D.; Cahntrell, R. W.; Serantes, D. Beyond the Blocking Model to Fit Nanoparticle ZFC/FC Magnetisation Curves. *Sci. Rep.* **2018**, *8*, 11166.

(61) Kamazawa, K.; Tsunoda, Y.; Kadowaki, H.; Kohn, K. Magnetic Neutron Scattering Measurements on a Single Crystal of Frustrated $ZnFe_2O_4$. *Phys. Rev. B* **2003**, *68*, 024412.

(62) Raghavender, A. T.; Hong, N. H. Dependence of Néel Temperature on the Particle Size of $MnFe_2O_4$. *J. Magn. Magn. Mater.* **2011**, *323*, 2145−2147.

(63) Rinaldi-Montes, N.; Gorria, P.; Martínez-Blanco, D.; Fuertes, A. B.; Puente-Orench, I.; Olivi, L.; Blanco, J. A. Size Effects on the Néel Temperature of Antiferromagnetic NiO Nanoparticles. *AIP Adv.* **2016**, *6*, No. 056104.

(64) Binder, K. Statistical Mechanics of Finite Three-Dimensional Ising Models. *Physica* **1972**, *62*, 508−526.

(65) Kuimova, M. K.; Yahioglu, G.; Levitt, J. A.; Suhling, K. Molecular Rotor Measures Viscosity of Live Cells via Fluorescence Lifetime Imaging. *J. Am. Chem. Soc.* **2008**, *130*, 6672−6673.